Research Article | Vol. 12, No. 7 / 1 July 2021 / Biomedical Optics Express 3965
Biomedical Optics EXPRESS

Space curvature-inspired nanoplasmonic sensor for breast cancer extracellular vesicle fingerprinting and machine learning classification

MOHAMMADRAHIM KAZEMZADEH,[1,2,9] COLIN L. HISEY,[3,4,9] ANASTASIIA ARTUYANTS,[3,4] CHERIE BLENKIRON,[5,6] LAWRENCE W. CHAMLEY,[3,4] KAMRAN ZARGAR-SHOSHTARI,[7] WEILIANG XU,[1,2] AND NEIL G. R. BRODERICK[2,8,*]

[1]*Department of Mechanical Engineering, University of Auckland, Auckland 1010, New Zealand*
[2]*Dodd-Walls Centre for Photonic and Quantum Technologies, New Zealand*
[3]*Department of Obstetrics and Gynaecology, University of Auckland, Auckland, 1023, New Zealand*
[4]*Hub for Extracellular Vesicle Investigations, University of Auckland, Auckland 1023, New Zealand*
[5]*Department of Molecular Medicine and Pathology, University of Auckland, Auckland 1023, New Zealand*
[6]*Auckland Cancer Society Research Centre, University of Auckland, Auckland 1023, New Zealand*
[7]*Department of Surgery, University of Auckland, Auckland 1023, New Zealand*
[8]*Department of Physics, University of Auckland, Auckland 1010, New Zealand*
[9]*Authors contributed equally*
[*]*n.broderick@auckland.ac.nz*

Abstract: Extracellular vesicles (EVs) are micro and nanoscale lipid-enclosed packages that have shown potential as liquid biopsy targets for cancer because their structure and contents reflect their cell of origin. However, progress towards the clinical applications of EVs has been hindered due to the low abundance of disease-specific EVs compared to EVs from healthy cells; such applications thus require highly sensitive and adaptable characterization tools. To address this obstacle, we designed and fabricated a novel space curvature-inspired surfaced-enhanced Raman spectroscopy (SERS) substrate and tested its capabilities using bioreactor-produced and size exclusion chromatography-purified breast cancer EVs of three different subtypes. Our findings demonstrate the platform's ability to effectively fingerprint and efficiently classify, for the first time, three distinct subtypes of breast cancer EVs following the application of machine learning algorithms on the acquired spectra. This platform and characterization approach will enhance the viability of EVs and nanoplasmonic sensors towards clinical utility for breast cancer and many other applications to improve human health.

1. Introduction

Raman scattering is an inelastic form of light scattering that can provide information about the chemical bonds present in the scattering material. The obtained spectra can then be used as a unique fingerprint of the material, enabling many successful applications in biological sensing including cancer detection and classification [1–3]. However, conventional Raman spectroscopy requires a relatively abundant sample and long signal acquisition times to provide accurate results due to the low probability of the inelastic scattering. This has hindered the utility of Raman spectroscopy for many applications, particularly in clinical scenarios where sample amounts are limited and long signal acquisition times are impractical.

Surface-enhanced Raman Spectroscopy (SERS) [4] is a powerful sensing method capable of increasing the degree of Raman scattering by many orders of magnitude, drastically improving its potential for use in applications involving limited or rare samples. SERS works by exploiting

#428302 https://doi.org/10.1364/BOE.428302
Journal © 2021 Received 20 Apr 2021; revised 24 May 2021; accepted 27 May 2021; published 9 Jun 2021

Biomedical Optics EXPRESS

plasmonic resonances at the substrate surface which can enhance the local intensity of light and thus the amplitude of the Raman signal [5,6]. Since the first demonstration of SERS, significant work has been done to find the optimum geometric structure for SERS substrates [7–10], indicating the importance of nanoscale features. To have precise control over the nanostructure geometry, most of these fabrication methods use different types of nanometric lithography such as electron-beam lithography (EBL) [11,12], focused ion beam (FIB) [13–15] and combinations of soft and nanoparticle lithography [16–18]. Soft and nanoparticle lithography are mostly preferred to their counterparts (EBL, FIB) as they more easily achieve three dimensional structures and do not require sophisticated equipment, making them more accessible and less expensive. For instance, nanometric beads in polydimethylsiloxane (PDMS) have been coated in silver to fabricate three dimensional nanobowl SERS structures [18,19].

A novel technique for SERS design and fabrication based on the notion of transformation optics [6,20] has also been explored by several groups [21], demonstrating that the substrate curvature can further enhance the Raman signal. This was achieved by coating the surface of polystyrene nanoparticles with gold. After dissolving polystyrene, the curved gold plate was transferred to another substrate and silver nanoparticles were added to the gold surface using cluster beam deposition [22]. Sensitivity down to single molecule detection was achieved, but as a significant portion of this enhancement was due to the plasmonic interaction of silver nanoparticles, it again suffers from weak chemical stability. The fabrication of such structures is also very complicated and the final mechanical stability is low due to the weak adhesion of the transferred gold layer to the new substrate.

As a result of these advances in SERS substrate fabrication and signal amplification, applications involving rare or limited biological samples have become more clinically viable. One promising type of SERS analysis with rapidly growing interest involves cancer detection and identification by using extracellular vesicles (EVs) as liquid biopsy markers. EVs are micro and nanoscale lipid-enclosed packages that circulate in all bodily fluids and their cargo are indicative of their cell of origin. Establishing the Raman spectra of cancer-specific EVs may be useful in diagnosis or treatment monitoring, and different methods of SERS detection have been used for the characterization of cancer EVs and other biological applications. These generally fall into two main categories including labeled, where substrates are functionalized with probes that target specific antigens on the EV surface using antibodies, aptamers, or peptides [23–28], and label-free [19,29–33].

Regarding breast cancer, SERS has been used in several studies to distinguish cancerous and noncancerous cells [34–37], while only a few recent proof-of-concept studies have examined the classification potential for EVs. One study successfully classified MCF-10A (nontumorigenic breast epithelium) and MDA-MB-231 (triple negative breast cancer) EVs using a novel nata de coco-based silver nanoparticle hybrid material following standard cell culture with EV-depleted serum and subsequent density gradient purification [38]. However, while density gradient purification is a well-established and highly effective method for removing non-EV contaminants, the depletion of exogenous bovine EVs from serum supplements using ultracentrifugation is known to be only partially effective [39], and the remaining bovine EVs may convolute the acquired EV spectra. In another study, EVs from MCF-7 (ER+/PR+), MDA-MB-231, and MCF-10A cells grown in commercially available EV-depleted serum and isolated by repeated ultracentrifugation were successfully classified by gold colloid SERS [40]. However, protein and other co-precipitated contaminants are known to persist even after repeated ultracentrifugation steps with a great cost to total EV yield [41], again potentially confounding the acquired spectra and strongly encouraging further studies which mitigate these issues. In addition, no study has yet obtained spectra nor classified breast cancer EVs from HER2-positive cells, an important subtype used in clinical breast cancer scenarios.

Biomedical Optics EXPRESS

As EVs consist of non-chromophore biomolecules, they naturally have a very low SERS signal [42] and furthermore due to the relatively large size of EVs (30-150+ nm) and the small active SERS distance of plasmonic particles (usually less than 5 nm), the use of plasmonic nanoparticles and unlabelled EVs is problematic and unlikely to generate strong SERS signals [43]. On the other hand, labeled SERS can be used to selectively isolate and characterise specific subtypes of EVs from complex mixtures, but the labels can inhibit the access of EVs to the plasmonic surface and the obtained spectra may lack valuable information about the biomolecular contents of the captured EVs. Thus efficient identification and characterisation of EVs at low concentrations using SERS is still an ongoing challenge.

In this study, we expand on these recent efforts by designing, fabricating, and testing a space-curvature inspired SERS substrate composed of a tightly packed nanocup pattern with improved granularity on its gold surface. We prove both numerically and analytically, that in combination, these geometric features significantly increase the SERS enhancement for chemical species and are particularly amenable for label-free biological applications such as EV characterization. This highly effective structure is also readily accessible compared to many other reported SERS substrates, requiring only nanoparticle and soft lithography followed by a two step sputter deposition of gold. In addition, the use of CELLine adherent bioreactors allowed the production of vast numbers of EVs compared to conventional cultures, without the risk of contamination with exogenous bovine serum EVs, while size exclusion chromatography provided a simple and effective method for removing contaminating proteins. Finally, we explore the substrate's potential utility in biomedical applications by classifying, for the first time, three distinct subtypes of breast cancer EVs by applying several machine learning algorithms to the acquired spectra.

2. Methodology

Our surface is designed using transformation optics to achieve extremely high electric fields around nanometric surface features. The main idea is that the gradient index material conjugated with the normal plasmonic waveguide can first increase the wave coupling from the incident laser into the plasmonic surface [44] and second, the presence of the material distribution can help the propagated plasmonic wave confine near the material gradient so that it propagates for longer distances [45]. Both of these statements have been proven semi-analytically using coupled mode theory [46]. However, material gradients cannot be directly used around a SERS surface as it would prevent the investigated analyte from reaching the surface where the maximum electromagnetic wave confinement and resulting maximum Raman enhancement exist. Transformation optics can be applied to solve this problem by transforming the material gradient into a curvature in space without changing the behaviour of the electric field. This is the reverse process of the usual applications of transformation optics in which the physical effects of space curvature are implemented by material distribution.

2.1. Design method

Consider a relative permittivity and permeability distribution of $\varepsilon_{\varphi\varphi}$ and $\mu_{\varphi\varphi}$ as shown in Fig. 1(a). This material is placed on top of a flat metallic surface and also has rotational symmetry along the vertical z axis as illustrated in Fig. 1(a). Theoretically, any plasmonic nanoparticle placed inside this area will create a resonant electric field with significantly higher amplitude than a bare particle. However, any high index material will prevent the analyte from reaching the surface of the particle where we have the maximum electric field and hence the highest Raman emission. We can apply the reverse method of transformation optics to turn this material gradient into a curved empty space so that particle is not surrounded by any material. As we have cylindrical symmetry, quasi-conformal transformation optics [47] can be applied. The detailed process of this reverse transformation was previously described [20,48]. This transformation changes

Biomedical Optics EXPRESS

the flat substrate into a surface with constant curvature as illustrated in Fig. 1(b). By placing a nanoparticle in the curved substrate we have the benefit of further amplification of the resonant field while the analyte can freely reach the nanoparticle surface.

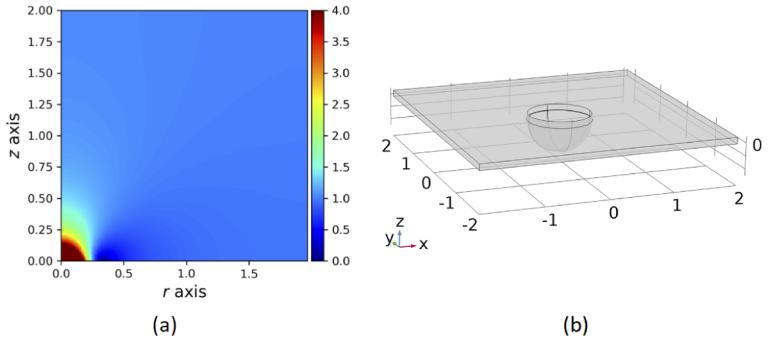

Fig. 1. (a) $\varepsilon_{\varphi\varphi}$ and $\mu_{\varphi\varphi}$ distribution in R-Z plain (b) curvature that can mimic the material distribution in (a)

COMSOL Multiphysics was used to model this concept by simulating different scenarios in which a gold nanoparticle with variable size is placed on either a flat or curved gold substrate as shown in Fig. 2(a) and (b). This plasmonic structure was illuminated with 785 nm light from the top and we solved for the resulting electric field. The amplitude of the normalized electric fields relative to the incident field for the flat and curved substrate are shown in Fig. 2(c) and (d), respectively. It can be seen that the electric field around the nanoparticle is enhanced in both cases while the size of the hot-spot is clearly significantly bigger for the curved substrate. However, for a quantitative assessment, the volumetric average of the normalized electric field in the hotspot area (area which is marked by the blue cylinder at the contact point of spherical nanoparticle and substrate (Figs. 2(a) and (b)) is calculated.

The result for the flat and curved substrates, when various thicknesses of the substrate and sizes of nanoparticles were considered, are shown in Fig. 3(a) and (b), respectively. The electric field enhancement ratio is also demonstrated in Fig. 3(c). As expected the average electric field is enhanced for almost all values for the thickness of substrate and the size of nanoparticle.

It should be noted that these simulations do not accurately model the small region where the ideal nanoparticle touches the substrate due to the minimum meshing size [6]. This may cause some error in the results in this region but as this is a localized effect it does not significantly alter our results. Furthermore, such idealized shapes are impossible to fabricate and in fact the Finite Element Model (FEM) shape could be a more realistic approximation compared to our ideal model. This problem has been addressed analytically for structures smaller than 200 nm in [6,49] and we have also attempted to solve this problem for the larger structures by introducing a novel simulation method [50,51].

Knowing the expected electric field distribution allows the calculation of the expected Raman enhancement using the method in [5]. They demonstrated that the Raman enhancement is proportional to the amplitude of the enhanced field near the plasmonic structures divided by the amplitude of the incident electric field, all to the fourth power. This expected enhancement is shown in Fig. 4(a) along with the improvement compared to the flat substrate in (b) for a range of different designs. The amount of enhancement for flat and curved substrate is found to be between 1 to 3 orders of magnitude higher for some nanoparticle sizes and the substrate thicknesses. To show the effect of the substrate radius of curvature on Raman enhancement, we also simulated the scenario in which the nanoparticle radius was chosen to be 20 nm with 10 nm substrate thickness and we varied the radius of substrate curvature between 250 nm to 750 nm. The calculated ratio of Raman enhancement between the flat and curved substrate for

Biomedical Optics EXPRESS

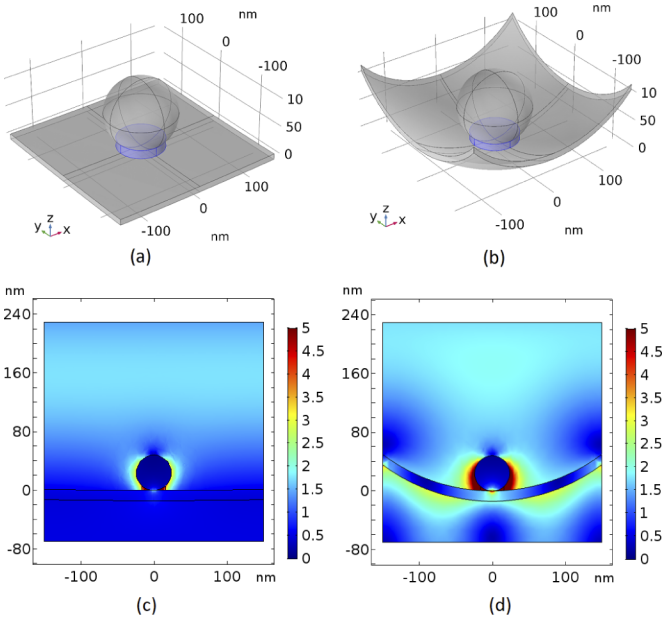

Fig. 2. A spherical nanoparticle on (a) flat and (b) wrapped substrates, and normalized electric field distributions around the nanoparticle in (c) flat and (d) wrapped substrate.

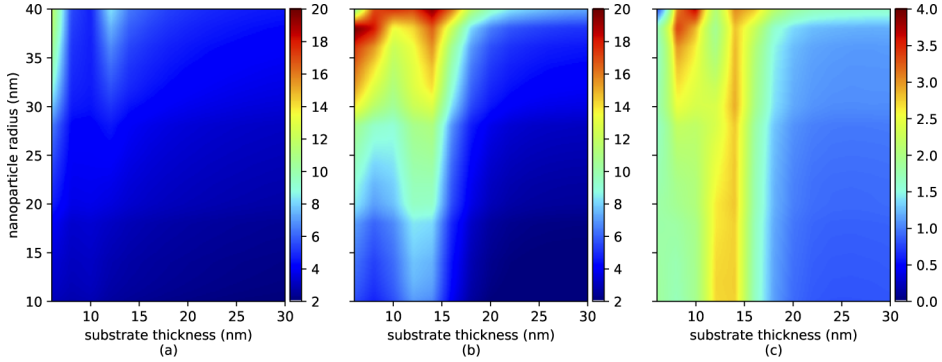

Fig. 3. Volumetric average (a) and (b) of normalized electric field in the designated hotspot in Fig. 2(a) and (b) for the flat and wrapped substrate, respectively, and (c) The ratio of (b) to (a).

this scenario is shown in Fig. 4(c). To clearly demonstrate that this enhancement is due to the curvature of the substrate and not the nanoparticle, we also simulated a cubic nanoparticle for both a flat and curved substrate, as is shown in Fig. 5 and again the curved substrate results in a significantly higher electric field.

2.2. Nano fabrication

A combination of soft and nanoparticle lithography were used to fabricate the described warped substrate. First, a cleaned positively charged glass slide was washed with acetone followed by isopropyl alcohol to remove any residue from the glass surface. Then, the glass slide was oxygen plasma treated using radio frequency reactive ion etching(50W 50% Oxygen inlet 300s, Nordson March CS-1701). This process adds OH^{-1} to the surface of the glass and makes it hydrophilic.

Biomedical Optics EXPRESS

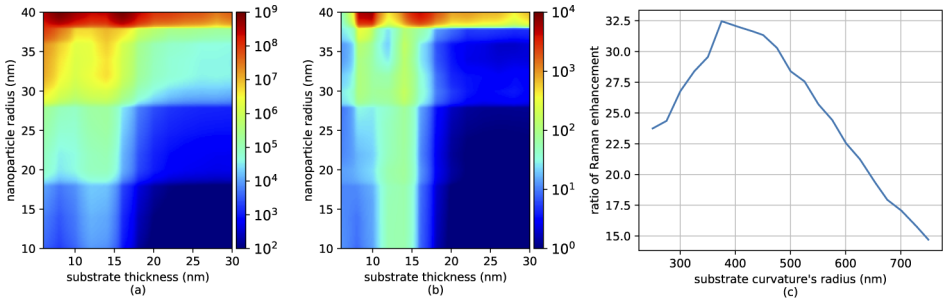

Fig. 4. (a) Expected Raman enhancement by the wrapped substrate, (b) the ratio of expected Raman enhancement of Wrapped to flat substrate, and (c) the effect of the radius of the curvature in Raman enhancement.

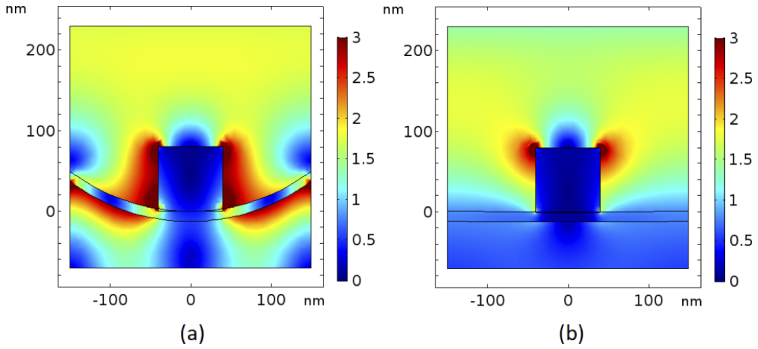

Fig. 5. The distribution of normalized electric field around the cubic nanoparticle in the (a) flat and (b) wrapped substrates.

A suspension of $1\mu m$ polystyrene beads (89904-5ML-F, SigmaAldrich) was diluted to the ratio of 5 percent solid in ultrapure MilliQ water and sonicated for one hour to avoid any aggregation in suspension. Then 50 μl of the prepared suspension was dropped on the oxygen plasma cleaned glass slide. The glass slide was gently tilted until a uniform spread of suspension was achieved on the top surface. Then, the suspension was dried in a controlled environment at 25^{o}C and 60% humidity while the slide was placed on a surface with 10 degree slope from horizontal. We have found that this process is more efficient than Langmuir and spin coating to fabricate a large number of samples. Large areas of mono layer beads with sizes around few millimeter square especially in the middle of glass slides can be achieved using this method. The dried glass slide is then put in an oven at 65^{o}C to completely dry the slide and increase the adhesion of beads to the glass surface.

Next, we created a negative mold of the beads using PDMS (Sylgard 184, Dow) mixed with its curing agent at a 10:1 ratio. The PDMS was degassed to remove bubbles, then poured onto the prepared glass slide with a thickness of 1 mm, and degassed again. After being baked at 65^o C for 2 hours, the PDMS was gently peeled from the glass slide with some beads typically remaining stuck to the PDMS. Any remaining beads were removed from the PDMS using an acetone sonication bath for 15 minutes. Acetone does not change the surface structure but it diffuses into the PDMS causing it to swell up. This effect can be reversed by putting the PDMS in an oven for 24 hours at 100^{o}C. This thermal processing also improves the subsequent gold coating leading to cleaner gold on the surface of PDMS.

The resulting PDMS surface was gold coated using direct current sputtering with a 99.99% pure gold target. The coating process was done with the rate of 0.5 nm per minute until a 12.5 nm

Biomedical Optics EXPRESS

thickness was achieved then the deposition rate was increased to 6 nm per minute (Q150R S, Quorum). This method first provides a uniform layer on the PDMS surface, then the higher deposition rate leads to a larger grain size of the gold at the top of the structure. We used this sputtering setting based on the simulation results in Fig. 4. The overall process of the fabrication is depicted in Fig. 6.

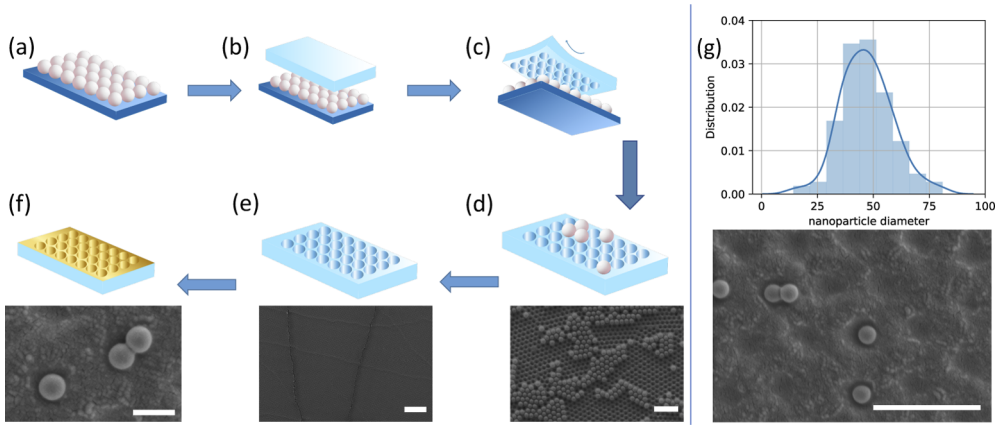

Fig. 6. Nanobead and soft lithography fabrication shematic showing (a) nanoparticle deposition on a cleaned and processed glass slide, (b) pouring PDMS on deposited nanoparticles, (c) peeling off the cured PDMS, (d) cleaning the resulting PDMS mold of nanoparticles (scale bar = 5 μm), (e) resulting PDMS mold after cleaning (scale bar = 20 μm), (f) two step sputter deposition of gold with trapping of 300 nm beads to represent EVs (scale bar = 500 nm), (g) size distribution of generated gold nanoparticles using two step gold deposition (scale bar = 2 μm)

2.3. Bioreactor culture and EV isolation

One of the several schemes used to classify breast cancer includes the receptor status of the cells, including estrogen receptor (ER), progesterone receptor (PR), and human epidermal growth factor receptor 2 (HER2). In this study, for the first time, EVs from three different cell lines representing different subtypes on the breast cancer spectrum, including MCF-7 (ER+/PR+/HER2-), BT-474 (ER+/PR+/HER2+) and BT-20 (triple negative) [52], were cultured in CELLine AD 1000 bioreactor flasks as previously described [53] and used for SERS analysis. Briefly, cells were seeded in the cell chamber in DMEM (Gibco) with 10% FBS (Merck) and 1% Pen/Strep (Gibco) and gradually adapted to Advanced DMEM/F-12 (Gibco) with 2% CDM-HD (Fibercell), 1% Glutamax (Gibco), and 1% Pen/Strep (Gibco) over the course of 4 weeks. To isolate EVs, the 15 ml of conditioned media from the cell chamber of the bioreactor was centrifuged at 2,000 xg for 10 min to remove cells and other debris. The supernatant was then centrifuged at 10,000 xg for 30 min (JA.30-50 Ti rotor, Avanti, Beckman Coulter) to pellet the large EVs (also known as microvesicles). This supernatant was then ultracentrifuged at 100,000 xg for 70 min (JA.30-50 Ti rotor, Avanti, Beckman Coulter) to yield a crude small EV pellet (also known as nanovesicles). This pellet was resuspended in 700 µl PBS and stored at -80 C until needed.

500 µl of the crude small EV suspension was purified by loading it onto a 35 nm qEV Original size exclusion chromatography column (SEC, Izon) and fractions 7 through 26 were collected using an automated fraction collector (Izon, 500 µl per fraction). High-Sensitivity BCA assay (Pierce, ThermoFisher Scientific) was performed for each of the collected fractions to determine their protein concentration.

Biomedical Optics EXPRESS

2.4. EV characterization

SEC-purified small EV fractions were diluted in Phosphate buffered saline (PBS) at a 1:100 ratio and measured with a NS300 Nanosight (Malvern Panalytical). Three 30 second videos were taken under low flow conditions (Screen gain:2, Camera level:8) and characterized using the Nanosight 3.4 software (Screen gain:10, Detection threshold:7) to calculate mean and mode particle diameters, concentration, and size distributions of each fraction. These results, combined with protein amounts from the BCA assay were used to determine the EV-rich, protein-contaminant poor fractions, which were then pooled for SERS and transmission electron microscopy (TEM). These pooled fractions were also then characterized using NTA and BCA.

Prior to TEM or SERS, EV samples were transferred from PBS buffer to ultrapure water by loading 500 μl of the purified small EVs into a Vivaspin 500 (Sartorius) centrifugal concentrator with a 100 kDa cutoff and spun at 10,000 xg until most of the PBS had flowed through the filter (roughly 10 min). 450 μl of ultrapure water was then added to the filter and the centrifugation process was repeated twice more before finally suspending the EVs in 100 μl ultrapure water. This preparation step is critical for both TEM and SERS to reduce the presence of salt crystals following dehydration of the sample.

Negative staining TEM of purified small EVs was conducted by adsorption onto Formvar-coated copper grids (Electron Microscopy Sciences) for 5 min. Excess liquid was removed with filter paper (Whatman) and the copper grid was then transferred to 20 μL of 2% uranyl acetate for 2 min. Excess liquid was again removed with filter paper and the grid was allowed to dry under a lamp for 10 min. Grids were visualized on Tecnai G2 Spirit TWIN (FEI, Hillsboro, OR, USA) transmission electron microscope (TEM) at 120 kV accelerating voltage. Images were captured using a Morada digital camera (SIS GmbH, Munster, Germany).

3. Result and discussion

3.1. EV isolation and purification

EVs were effectively separated from contaminating proteins using size exclusion chromatography. EV-rich fractions, based on NTA and BCA data, were found to be 8-10 (green boxes) and were pooled and used for NTA, TEM and SERS (Fig. 7 A-C). NTA demonstrated the expected size distributions of purified small EVs from cell culture and TEM also showed a typical round morphology of the expected sizes (Fig. 7 D-F). Pooled EV samples (Fig. 7 G) were normalized to equal particle concentration using NTA measurements before loading onto SERS substrates.

The use of CELLine AD 1000 bioreactor cultures combined with SEC purification provided several advantages compared to previous studies in this field. First, the 10 kDa semi-permeable cellulose acetate membrane separating the 15 ml cell culture chamber from the 1 L media chamber allowed the use of 2% FBS in the media chamber and passive diffusion of waste products and smaller nutrients between chambers, while preventing exogenous FBS EVs from entering the cell chamber. In addition, the chemically defined CDM-HD serum replacement additive further supported growth of the high density culture. Often, EVs isolated from cultured cells are collected in one-off experiments, using large numbers of conventional flasks which require either inefficient FBS EV-depletion strategies or FBS starvation of the cultured cells, both of which could produce confounding factors in the final EV product. The bioreactors not only prevented these issues, but provided a much higher concentration of EVs in the conditioned media compared to conventional cultures due to the high cell density. In addition, the natural turnover of cells within the bioreactor culture allowed the consistent harvest of EVs twice per week over the course of up to five months (publication in progress) while replacing the media chamber only once per week. This allows more high-risk and creative experimental designs, such as the SERS fingerprinting and classification in this study, as the EVs are not seen as a limited or expensive reagent. The 15 ml of highly concentrated conditioned media also enables

Biomedical Optics EXPRESS

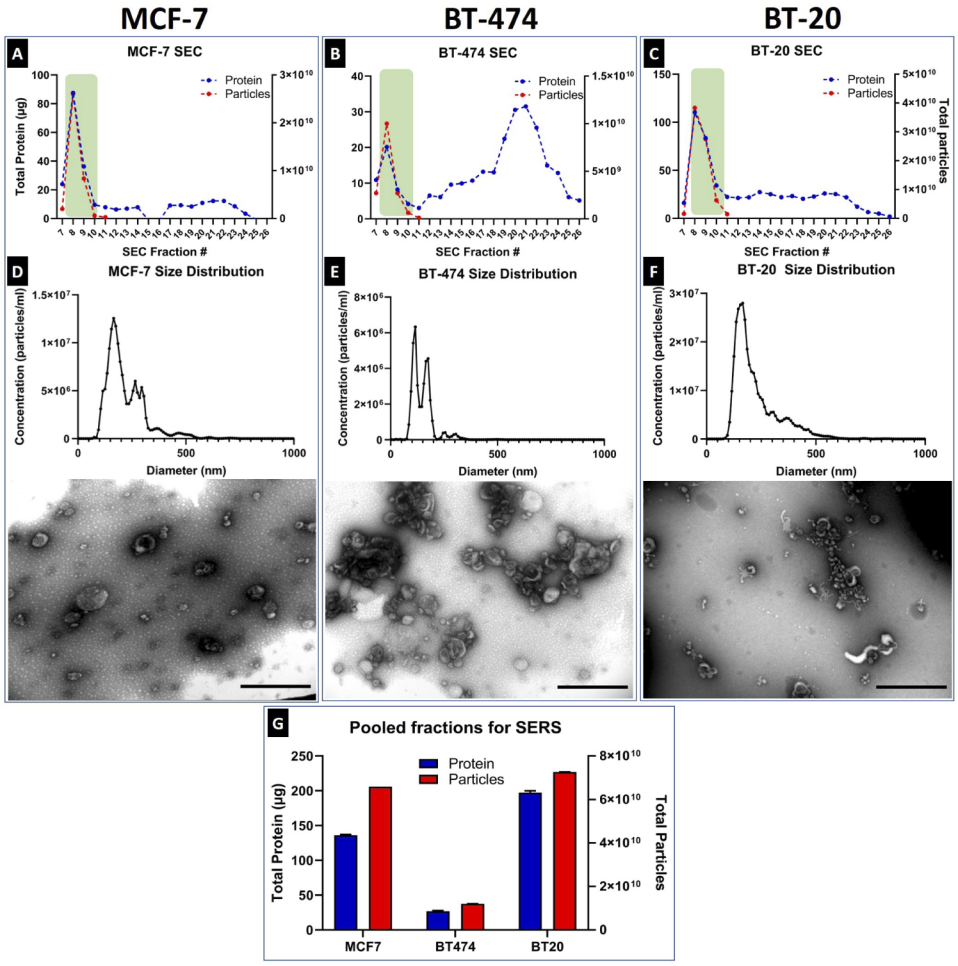

Fig. 7. Size exclusion chromatography purification of small EVs showing protein and particle amounts of each collected fraction for (A) MCF-7, (B) BT-474 and (C) BT-20. NTA size distributions and TEM images of pooled EV-rich fractions for (D) MCF-7, (E) BT-474 and (F) BT-20 small EVs (scale bars = 500 nm), (G) and pooled particle and protein counts for all three samples from a single isolation.

Biomedical Optics EXPRESS

several efficient and cost-effective purification workflows, which are essential for rigour and reproducibility as the EV SERS field continues to grow. In this experiment, for example, we chose to use ultracentrifugation as a concentration strategy to reduce the 15 ml volume to 500 μl, followed by loading the sample onto a small SEC column to remove contaminating proteins (Fig. 7 A-C). However, the initial 15 ml product could also be concentrated using ultrafiltration and used with a similar column, or even loaded directly onto a larger SEC column without concentration, depending on the equipment available.

3.2. Reproducibility test

The functionality of the designed surface was tested by obtaining Raman spectra from aqueous solutions of both Rhodamine b (Rb) and breast cancer EVs of different concentrations. Rb was used as a chemical standard to test the reproducibility of the designed SERS and also to determine the degree of Raman enhancement caused by the surface using our quick drying method, which is essential for EVs. Additionally, breast cancer EVs were investigated to demonstrate the potential of the fabricated SERS in cancer detection and classification. For the Raman measurements 1 μl per square millimetre of samples was dropped on the fabricated SERS and quickly dried at 40^{o} C until no water was observed on the surface. This minimizes the coffee ring effect and increases the uniformity of the analyte across the SERS substrate.

The Raman measurement was done using a Horiba LabRAM HR Evolution confocal Raman microscope using a 50X microscope object and 785 nm laser. The laser power was controlled using a neutral density filter and set to 5 to 10 percent of the maximum power (100 mW) depending on the sample type. All measurements were obtained with a 10s acquisition time and only one accumulation. Then, the baseline was established and noise was removed using asymmetric least squares smoothing established in [54].

Sixteen spectra obtained from three different concentrations of Rb are shown in Fig. 8(a), (b) and (c) for the concentrations of 10^{-4}, 10^{-5} and 10^{-6} M, respectively. The yellow area corresponds to the maximum and minimum of the obtained spectra in each Raman shifts also the standard deviation is represented using cyan color. The curved substrate could identify the peaks of Rb even at 10^{-6} M while the lowest concentration that can be detected using the flat SERS

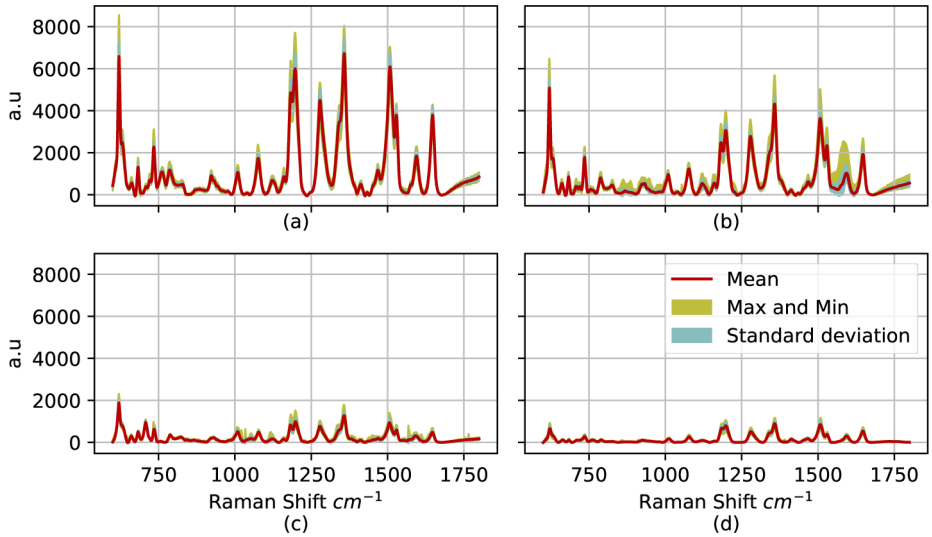

Fig. 8. The obtained Raman spectra of Rb with concentrations of (a) 10^{-4}M, (b) 10^{-5}M, and (c) 10^{-6}M using the curved SERS substrate, and (d) 10^{-5}M using flat SERS substrate.

Biomedical Optics EXPRESS

substrate was found to be 10^{-5} M with almost half of the peaks' height. This corresponds to around 20 times amplification achieved by the curvature of the substrate, as predicted in Fig. 4(b). Another important aspect of Fig. 8 is that it shows that the signal strength is directly related to the concentration, allowing quantification of the samples once a proper calibration has been done, which could also be incredibly valuable in biomedical applications.

To further test the reproducibility, Raman spectra of three replicates from the same BT-20 EVs with the concentration of $\approx 1 \times 10^{10}$ EVs/ml were obtained. Spectra from each sample were obtained from separately fabricated SERS and 25 measurements were done from 25 different and random points where the minimum distance of one laser spot size was maintained. The normalized spectra from these three separately fabricated SERS of small EVs from BT-20 cells are shown in Fig. 9(a)-(c). Again, excellent reproducibility can be seen giving us confidence that any variability between substrates does not significantly affect the spectra acquisition. We also attempted to obtain SERS spectra from BT-20 EVs using the flat SERS substrate. However, due to the weak enhancement achieved by the flat substrate and the smaller hotspot areas (see Figs. 2(c) and 5(b)), we were unable to obtain any meaningful spectra.

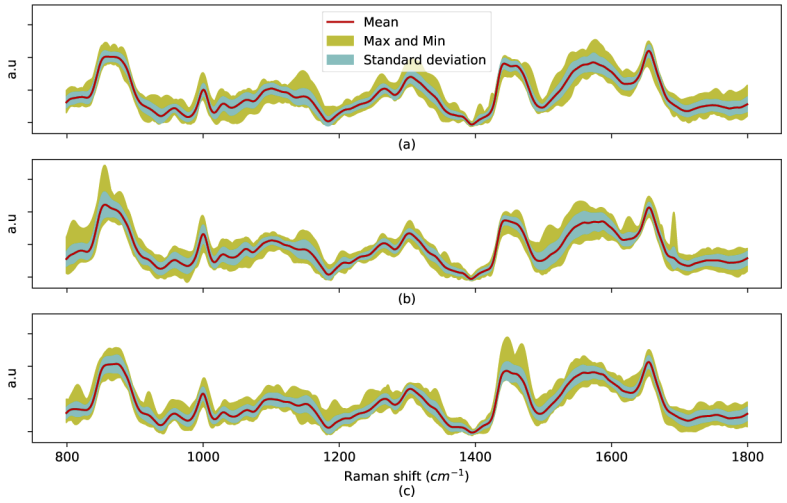

Fig. 9. Three replicates (a), (b) and (c) of BT-20 EV Raman spectra.

3.3. Effect of concentration on the Raman spectra

To demonstrate the effect of concentration on statistical analysis of the data we plotted the PCA of the normalized Rb data in Fig. 10. The normalization removes the amplitude of the signal but preserves the wavenumbers of the different peaks. Although the major peaks of Rb almost perfectly match in the spectra, the PCA analysis shows some difference between samples. There are number of reasons for this such as the contamination during the fabrication process and the difference in molecular orientation in hotspot areas due to the different speed of crystallization on the SERS surface. In fact, there is always some small amount of contamination on the substrates due to impurities of gold target, PDMS burning due to the DC sputtering and the solution drying process. The other major reason is the difference in the drying speed which leads to the presence of water in tiny geometrical features on SERS surface. This effect has been investigated in detail for drying of EV solution and its corresponding effects on Raman spectra in [19].

The effect of concentration was also investigated for the EVs spectra in this work. The small EV solution from BT-20 cells was diluted to a concentration of $\approx 1x10^9$ EVs/ml and the spectra were obtained from 100 random points on the SERS surface. For the sake of clarity, 30 spectra

Biomedical Optics EXPRESS

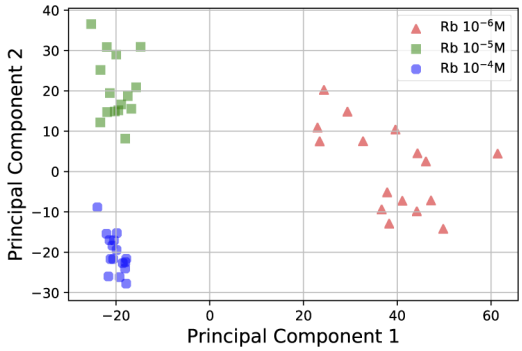

Fig. 10. 2D PCA transformation of the normalized spectra of Rb in Fig. 8.

of each of the 1x10^9 and 1x10^{10} concentrations are shown in Fig. 11(a), and the PCA analysis is depicted in Fig. 11(b). Similar to the Rb spectra, there are some differences between the spectra using PCA, although the location of the major peaks remain the same.

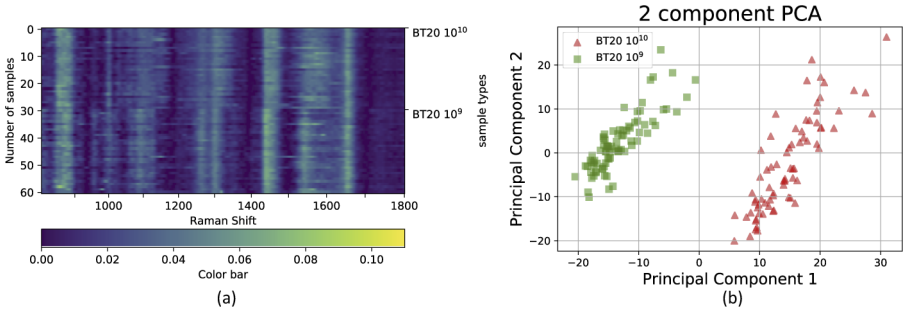

Fig. 11. Normalized Raman spectra of (a) BT-20 cell line with different ($\approx 1x10^{10}$ and $\approx 1x10^9$ EVs/ml) concentrations, and (b) 2D PCA transformation of the BT-20 EV spectra with different concentrations.

Next, the Raman spectra of EVs from two cell lines of other breast cancer subtypes, MCF-7 and BT-474, were obtained with equal concentration of $\approx 1x10^{10}$ to investigate the classification potential using the proposed sensor. The average spectra of each type of breast cancer EV are shown in Fig. 12. In this figure the mean, maximum/minimum and standard deviation are shown in red, yellow and cyan color, respectively and it can be seen that the sensor provides excellent reproducibility as before. In addition, each prominent band has been labelled according to the biochemical substance responsible for the peak following the analysis of Movasaghi *et al.* [55]. The PCA analysis of these spectra is shown in Fig. 13(a). As can be seen, each breast cancer subtype can be easily distinguished leading to accurate classification using several algorithms.

As a demonstration of the potential of our method we used the same PCA transformation developed for the high concentration samples on the spectra of BT-20 EVs with concentration of $\approx 1 \times 10^9$ (i.e. ten times lower) and plotted the results in Fig. 13(b) along with the original data. As expected, the BT-20 EV spectra with different concentrations lie almost on top of each other and are well separated from the spectra of EVs from the other breast cancer subtypes. This is important as it shows that our method can robustly classify breast cancer types irrespective of EV concentrations. Compared to patient plasma samples, which have reported EV concentration ranges anywhere from $\approx \times 10^7$ to $\approx \times 10^{13}$ EVs/ml and an average of $\approx 2 \times 10^{10}$ EVs/ml based on a careful review of the literature [56], the 20 μl of of $\approx 1 \times 10^9$ EVs/ml clearly indicates that this

Biomedical Optics EXPRESS

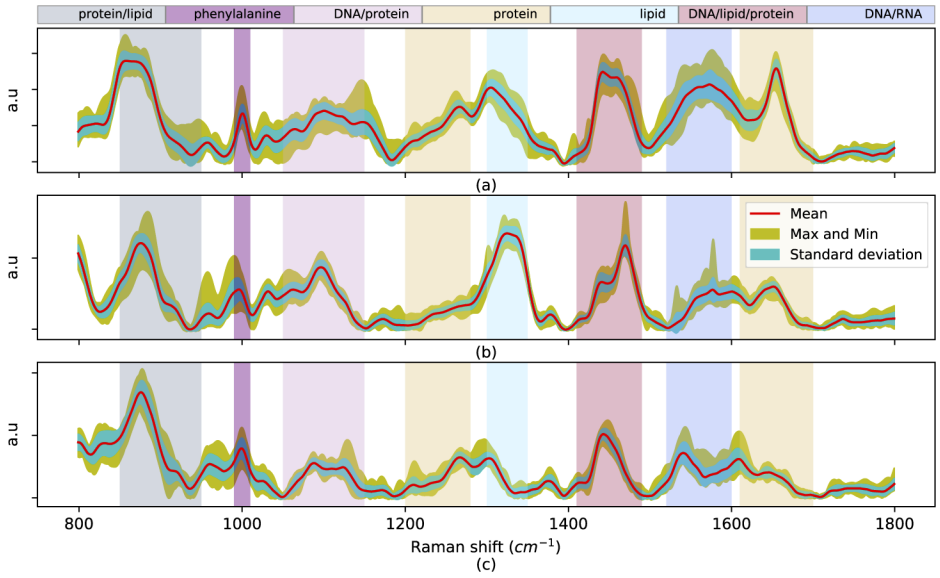

Fig. 12. Normalized Raman spectra of (a) BT-20, (b) BT-474 and (c) MCF-7 EVs with their specified band for each type of biomolecule.

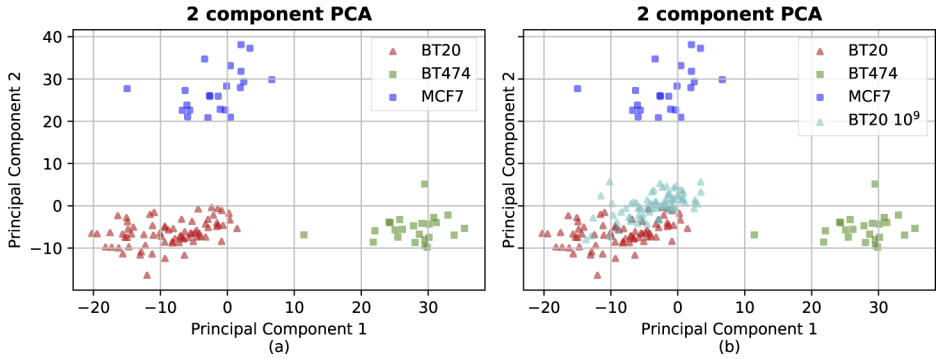

Fig. 13. 2D PCA transformation of (a) EV spectra from BT-20, BT-474 and MCF-7 EVs with the concentration of $\approx 1 \times 10^{10}$ EVs/ml, and transformation of Raman spectra of (b) BT-20 cell line EVs with the concentration of $\approx 1 \times 10^{9}$ when it is transformed by the obtained transformation in (a).

approach is clinically viable. Often, 500 μl to 2 ml of plasma can be obtained per patient, and the number of EVs from that sample that would be analysed using SERS is highly dependent on any pre-purification steps, the specific patient, and whether the whole EV population is analysed or only a disease-specific subset of EVs.

To properly test our classification scheme, we applied six different classification algorithms, all trained on the high concentration samples within our data set. The algorithms used were: C support vector classifier with RBF kernel (CSV), k-nearest neighbours (KNN), linear discriminant analysis (LDA), Random forest (RF), Gaussian process classifier (GPC), and decision tree (DT). The results are shown in Fig. 14 with the probability of each point in PCA plane to be BT-20 being represented using a color map. All the chosen classification algorithms successfully identify all the EV spectra correctly including BT-20 at a lower concentration. This shows the power of this sensor to classify the EVs at lower concentration, which is 100 times more sensitive than

Biomedical Optics EXPRESS

ELISA, a standardized fluorescence or absorbance-based microplate assay usually performed using antibody-conjugates [31].

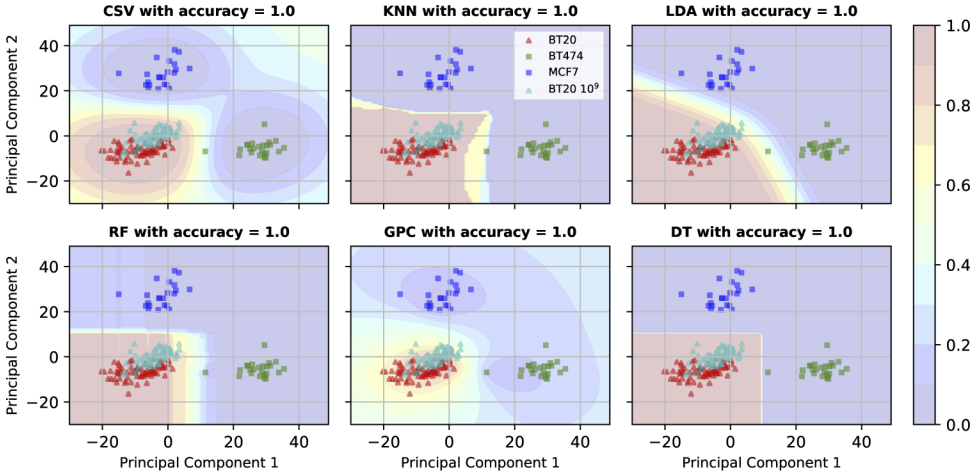

Fig. 14. Probability distribution in 2D PCA plain obtained using CSV, KNN, LDA, RF, GPC and DT classifiers.

4. Conclusion

In this study, we demonstrate the use of a novel space curvature-inspired and label-free SERS substrate for the classification of EVs of three distinct breast cancer subtypes with varying concentrations. Culturing the various cell lines in CELLine AD 1000 bioreactors enabled the isolation of copious amounts of EVs that are cultured in physiologically relevant conditions and which could be rapidly purified from contaminating proteins using automated size exclusion chromatography. Due to the incredibly high yields, we were able to demonstrate the minimal dependence of the Raman spectra on EV concentration over several orders of magnitude. In addition, clear differences in the averaged Raman spectra allowed the rapid classification of breast cancer subtypes using machine learning algorithms.

It is important to note that these are highly homogenous and purified samples compared to patient samples, in which the number of breast cancer EVs relative to other cell type-derived EVs could be very limited. However, these results serve as a proof of concept that, given sufficiently specific upstream isolation technology, either directly on the SERS or using other platforms (e.g. affinity-based microfluidics), that the Raman spectra of EVs could serve as valuable diagnostic or monitoring tools in breast cancer and many other diseases.

Funding. Goodfellow Fund for the Support of Urological Research; Breast Cancer Foundation New Zealand Innovation and Technology Grant; Dodd-Walls Centre for Photonic and Quantum Technologies.

Acknowledgements. The authors would like to thank the Photon Factory and the Hub for Extracellular Vesicle Investigations at the University of Auckland, and The Dodd-Walls Centre for Photonic and Quantum Technologies for their technical support.

Disclosures. The authors declare no conflicts of interest.

Data availability. Data underlying the results presented in this paper are not publicly available at this time but may be obtained from the authors upon reasonable request.

References

1. A. T. Tu and A. Tu, *Raman Spectroscopy in Biology: Principles and Applications* (Wiley, 1982).

Biomedical Optics EXPRESS

2. M. Jermyn, K. Mok, J. Mercier, J. Desroches, J. Pichette, K. Saint-Arnaud, L. Bernstein, M.-C. Guiot, K. Petrecca, and F. Leblond, "Intraoperative brain cancer detection with raman spectroscopy in humans," Sci. Transl. Med. **7**(274), 274ra19 (2015).
3. H. Chen, X. Li, N. Broderick, Y. Liu, Y. Zhou, J. Han, and W. Xu, "Identification and characterization of bladder cancer by low-resolution fiber-optic Raman spectroscopy," J. Biophotonics **11**(9), e201800016 (2018).
4. P. L. Stiles, J. A. Dieringer, N. C. Shah, and R. P. Van Duyne, "Surface-enhanced Raman spectroscopy," Annu. Rev. Anal. Chem. **1**(1), 601–626 (2008).
5. F. J. García-Vidal and J. Pendry, "Collective theory for surface enhanced Raman scattering," Phys. Rev. Lett. **77**(6), 1163–1166 (1996).
6. J. Pendry, A. Aubry, D. Smith, and S. Maier, "Transformation optics and subwavelength control of light," Science **337**(6094), 549–552 (2012).
7. Z. Zeng, Y. Liu, and J. Wei, "Recent advances in surface-enhanced Raman spectroscopy (SERS): Finite-difference time-domain (FDTD) method for sers and sensing applications," TrAC Trends Anal. Chem. **75**, 162–173 (2016).
8. T. Hutter, S. R. Elliott, and S. Mahajan, "Optical fibre-tip probes for sers: numerical study for design considerations," Opt. Express **26**(12), 15539–15550 (2018).
9. S. Kessentini, D. Barchiesi, C. D'Andrea, A. Toma, N. Guillot, E. Di Fabrizio, B. Fazio, O. M. Marago, P. G. Gucciardi, and M. Lamy de la Chapelle, "Gold dimer nanoantenna with slanted gap for tunable lspr and improved SERS," J. Phys. Chem. C **118**(6), 3209–3219 (2014).
10. C. Tira, D. Tira, T. Simon, and S. Astilean, "Finite-difference time-domain (FDTD) design of gold nanoparticle chains with specific surface plasmon resonance," J. Mol. Struct. **1072**, 137–143 (2014).
11. M. Kahl, E. Voges, S. Kostrewa, C. Viets, and W. Hill, "Periodically structured metallic substrates for SERS," Sens. Actuators, B **51**(1-3), 285–291 (1998).
12. L. Petti, R. Capasso, M. Rippa, M. Pannico, P. La Manna, G. Peluso, A. Calarco, E. Bobeico, and P. Musto, "A plasmonic nanostructure fabricated by electron beam lithography as a sensitive and highly homogeneous SERS substrate for bio-sensing applications," Vib. Spectrosc. **82**, 22–30 (2016).
13. K. Sivashanmugan, J.-D. Liao, J.-W. You, and C.-L. Wu, "Focused-ion-beam-fabricated au/ag multilayered nanorod array as SERS-active substrate for virus strain detection," Sens. Actuators, B **181**, 361–367 (2013).
14. A. Dhawan, M. Gerhold, and T. Vo-Dinh, "Theoretical simulation and focused ion beam fabrication of gold nanostructures for surface-enhanced raman scattering (SERS)," Nanobiotechnol. **3**(3-4), 164–171 (2007).
15. T. Gao, Z. Xu, F. Fang, W. Gao, Q. Zhang, and X. Xu, "High performance surface-enhanced raman scattering substrates of Si-based au film developed by focused ion beam nanofabrication," Nanoscale Res. Lett. **7**(1), 399 (2012).
16. M. Cottat, N. Lidgi-Guigui, I. Tijunelyte, G. Barbillon, F. Hamouda, P. Gogol, A. Aassime, J.-M. Lourtioz, B. Bartenlian, and M. L. de la Chapelle, "Soft uv nanoimprint lithography-designed highly sensitive substrates for SERS detection," Nanoscale Res. Lett. **9**(1), 623 (2014).
17. G. L. Liu and L. P. Lee, "Nanowell surface enhanced raman scattering arrays fabricated by soft-lithography for label-free biomolecular detections in integrated microfluidics," Appl. Phys. Lett. **87**(7), 074101 (2005).
18. M. Kahraman, P. Daggumati, O. Kurtulus, E. Seker, and S. Wachsmann-Hogiu, "Fabrication and characterization of flexible and tunable plasmonic nanostructures," Sci. Rep. **3**(1), 3396 (2013).
19. C. Lee, R. P. Carney, S. Hazari, Z. J. Smith, A. Knudson, C. S. Robertson, K. S. Lam, and S. Wachsmann-Hogiu, "3D plasmonic nanobowl platform for the study of exosomes in solution," Nanoscale **7**(20), 9290–9297 (2015).
20. J. B. Pendry, D. Schurig, and D. R. Smith, "Controlling electromagnetic fields," Science **312**(5781), 1780–1782 (2006).
21. P. Mao, C. Liu, G. Favraud, Q. Chen, M. Han, A. Fratalocchi, and S. Zhang, "Broadband single molecule SERS detection designed by warped optical spaces," Nat. Commun. **9**(1), 1–8 (2018).
22. K. Wegner, P. Piseri, H. V. Tafreshi, and P. Milani, "Cluster beam deposition: a tool for nanoscale science and technology," J. Phys. D: Appl. Phys. **39**(22), R439–R459 (2006).
23. S. Zong, L. Wang, C. Chen, J. Lu, D. Zhu, Y. Zhang, Z. Wang, and Y. Cui, "Facile detection of tumor-derived exosomes using magnetic nanobeads and SERS nanoprobes," Anal. Methods **8**(25), 5001–5008 (2016).
24. C. Lee, R. Carney, K. Lam, and J. W. Chan, "SERS analysis of selectively captured exosomes using an integrin-specific peptide ligand," J. Raman Spectrosc. **48**(12), 1771–1776 (2017).
25. Y.-F. Tian, C.-F. Ning, F. He, B.-C. Yin, and B.-C. Ye, "Highly sensitive detection of exosomes by SERS using gold nanostar@ Raman reporter@ nanoshell structures modified with a bivalent cholesterol-labeled dna anchor," Analyst **143**(20), 4915–4922 (2018).
26. Z. Wang, S. Zong, Y. Wang, N. Li, L. Li, J. Lu, Z. Wang, B. Chen, and Y. Cui, "Screening and multiple detection of cancer exosomes using an SERS-based method," Nanoscale **10**(19), 9053–9062 (2018).
27. E. A. Kwizera, R. O'Connor, V. Vinduska, M. Williams, E. R. Butch, S. E. Snyder, X. Chen, and X. Huang, "Molecular detection and analysis of exosomes using surface-enhanced Raman scattering gold nanorods and a miniaturized device," Theranostics **8**(10), 2722–2738 (2018).
28. T.-D. Li, R. Zhang, H. Chen, Z.-P. Huang, X. Ye, H. Wang, A.-M. Deng, and J.-L. Kong, "An ultrasensitive polydopamine bi-functionalized SERS immunoassay for exosome-based diagnosis and classification of pancreatic cancer," Chem. Sci. **9**(24), 5372–5382 (2018).

Biomedical Optics EXPRESS

29. K. Sivashanmugan, W.-L. Huang, C.-H. Lin, J.-D. Liao, C.-C. Lin, W.-C. Su, and T.-C. Wen, "Bimetallic nanoplasmonic gap-mode SERS substrate for lung normal and cancer-derived exosomes detection," J. Taiwan Inst. Chem. Eng. **80**, 149–155 (2017).
30. L. Tirinato, F. Gentile, D. Di Mascolo, M. Coluccio, G. Das, C. Liberale, S. Pullano, G. Perozziello, M. Francardi, A. Accardo, F. De Angelis, P. Cadeloro, and E. Di Fabrizio, "SERS analysis on exosomes using super-hydrophobic surfaces," Microelectron. Eng. **97**, 337–340 (2012).
31. J. Park, M. Hwang, B. Choi, H. Jeong, J.-H. Jung, H. K. Kim, S. Hong, J.-H. Park, and Y. Choi, "Exosome classification by pattern analysis of surface-enhanced raman spectroscopy data for lung cancer diagnosis," Anal. Chem. **89**(12), 6695–6701 (2017).
32. H. Shin, H. Jeong, J. Park, S. Hong, and Y. Choi, "Correlation between cancerous exosomes and protein markers based on surface-enhanced raman spectroscopy (SERS) and principal component analysis (PCA)," ACS Sens. **3**(12), 2637–2643 (2018).
33. Z. Yan, S. Dutta, Z. Liu, X. Yu, N. Mesgarzadeh, F. Ji, G. Bitan, and Y.-H. Xie, "A label-free platform for identification of exosomes from different sources," ACS Sens. **4**(2), 488–497 (2019).
34. S. Cervo, E. Mansutti, G. Del Mistro, R. Spizzo, A. Colombatti, A. Steffan, V. Sergo, and A. Bonifacio, "SERS analysis of serum for detection of early and locally advanced breast cancer," Anal. Bioanal. Chem. **407**(24), 7503–7509 (2015).
35. J. Yang, Z. Wang, S. Zong, C. Song, R. Zhang, and Y. Cui, "Distinguishing breast cancer cells using surface-enhanced Raman scattering," Anal. Bioanal. Chem. **402**(3), 1093–1100 (2012).
36. A. Hernández-Arteaga, J. d. J. Z. Nava, E. S. Kolosovas-Machuca, J. J. Velázquez-Salazar, E. Vinogradova, M. José-Yacamán, and H. R. Navarro-Contreras, "Diagnosis of breast cancer by analysis of sialic acid concentrations in human saliva by surface-enhanced Raman spectroscopy of silver nanoparticles," Nano Res. **10**(11), 3662–3670 (2017).
37. V. Moisoiu, A. Socaciu, A. Stefancu, S. D. Iancu, I. Boros, C. D. Alecsa, C. Rachieriu, A. R. Chiorean, D. Eniu, N. Leopold, C. Socaciu, and D. T. Eniu, "Breast cancer diagnosis by surface-enhanced raman scattering (SERS) of urine," Appl. Sci. **9**(4), 806 (2019).
38. N. Ferreira, A. Marques, H. Águas, H. Bandarenka, R. Martins, C. Bodo, B. Costa-Silva, and E. Fortunato, "Label-free nanosensing platform for breast cancer exosome profiling," ACS Sens. **4**(8), 2073–2083 (2019).
39. B. M. Lehrich, Y. Liang, and M. S. Fiandaca, "Foetal bovine serum influence on in vitro extracellular vesicle analyses," J. Extracell. Vesicles **10**, e12061 (2021).
40. P. Zhang, L. Wang, Y. Fang, D. Zheng, T. Lin, and H. Wang, "Label-free exosomal detection and classification in rapid discriminating different cancer types based on specific raman phenotypes and multivariate statistical analysis," Molecules **24**(16), 2947 (2019).
41. J. Webber and A. Clayton, "How pure are your vesicles?" J. Extracell. Vesicles **2**(1), 19861 (2013). PMID: 24009896.
42. L.-J. Xu, C. Zong, X.-S. Zheng, P. Hu, J.-M. Feng, and B. Ren, "Label-free detection of native proteins by surface-enhanced raman spectroscopy using iodide-modified nanoparticles," Anal. Chem. **86**(4), 2238–2245 (2014).
43. H. Shin, D. Seo, and Y. Choi, "Extracellular vesicle identification using label-free surface-enhanced raman spectroscopy: detection and signal analysis strategies," Molecules **25**(21), 5209 (2020).
44. S. Sun, Q. He, S. Xiao, Q. Xu, X. Li, and L. Zhou, "Gradient-index meta-surfaces as a bridge linking propagating waves and surface waves," Nat. Mater. **11**(5), 426–431 (2012).
45. R. F. Oulton, V. J. Sorger, D. Genov, D. Pile, and X. Zhang, "A hybrid plasmonic waveguide for subwavelength confinement and long-range propagation," Nat. Photonics **2**(8), 496–500 (2008).
46. A. Yariv, "Coupled-mode theory for guided-wave optics," IEEE J. Quantum Electron. **9**(9), 919–933 (1973).
47. D.-H. Kwon, "Quasi-conformal transformation optics lenses for conformal arrays," IEEE Antennas Wirel. Propag. Lett. **11**, 1125–1128 (2012).
48. M. Kazemzadeh, N. Broderick, W. Xu, and K. Z. Shoshtari, "Design and optimization of broadband and transparent SERS based on transformation optics," in *SPIE Micro+ Nano Materials, Devices, and Applications 2019*, vol. 11201 (International Society for Optics and Photonics, 2019), p. 112011L.
49. Y. Luo, A. Aubry, and J. Pendry, "Electromagnetic contribution to surface-enhanced raman scattering from rough metal surfaces: a transformation optics approach," Phys. Rev. B **83**(15), 155422 (2011).
50. M. Kazemzadeh, W. Xu, and N. G. Broderick, "Faster and more accurate time domain electromagnetic simulation using space transformation," IEEE Photonics J. **12**(4), 1–13 (2020).
51. M. Kazemzadeh, N. Broderick, and W. Xu, "Novel time-domain electromagnetic simulation using triangular meshes by applying space curvature," IEEE Open J. Antennas Propag. **1**, 387–395 (2020).
52. X. Dai, H. Cheng, Z. Bai, and J. Li, "Breast cancer cell line classification and its relevance with breast tumor subtyping," J. Cancer **8**(16), 3131–3141 (2017).
53. C. L. Hisey, P. Tomek, Y. N. Nursalim, L. W. Chamley, and E. Leung, "Towards establishing extracellular vesicle-associated RNAS as biomarkers for her2+ breast cancer," F1000Research **9**, 1362 (2020).
54. P. H. Eilers and H. F. Boelens, "Baseline correction with asymmetric least squares smoothing," Leiden University Medical Centre Report **1**, 5 (2005).
55. Z. Movasaghi, S. Rehman, and I. U. Rehman, "Raman spectroscopy of biological tissues," Appl. Spectrosc. Rev. **42**(5), 493–541 (2007).

Biomedical Optics EXPRESS

56. K. B. Johnsen, J. M. Gudbergsson, T. L. Andresen, and J. B. Simonsen, "What is the blood concentration of extracellular vesicles? implications for the use of extracellular vesicles as blood-borne biomarkers of cancer," Biochim. Biophys. Acta, Rev. Cancer **1871**(1), 109–116 (2019).